Optics Letters

Exploring nonlinearity-loss tradeoffs in foundry fabricated silicon integrated photon pair sources

Tom Dixon,[1] Yisbel Marin,[2,3] Imad I. Faruque,[4] and Krishna C. Balram[1,*]

[1]Quantum Engineering Technology Labs and School of Electrical, Electronic and Mechanical Engineering, University of Bristol, Bristol BS8 1UB, UK
[2]VTT Technical Research Centre of Finland Ltd., Tietotie 3, 02150 Espoo, Finland
[3]Current address: Lumiphase AG, Stäfa, Switzerland
[4]School of Mathematical and Physical Sciences, University of Sheffield, Sheffield, S10 2TN, UK
*krishna.coimbatorebalram@bristol.ac.uk

Received 18 November 2025; revised 18 December 2025; accepted 30 December 2025; posted 2 January 2026; published 27 January 2026

Foundry fabricated silicon heralded photon pair sources underpin a wide range of quantum photonics applications. Traditional photonics foundry platforms, originating in classical datacom applications, have waveguide cross-sections <0.2 μm^2, which significantly enhance surface absorption and roughness-induced scattering effects on propagating optical fields. Given the critical importance of loss for quantum information applications, here we consider the generation of photon pairs in a low-loss, thick (3 μm) silicon foundry platform and explore the associated nonlinearity-loss-footprint tradeoffs, with a view toward understanding the optimal silicon thickness for resonator-based photon pair sources.

https://doi.org/10.1364/OL.585144

Integrated quantum photonics platforms [1], which combine quantum optical state generation, manipulation and detection in chipscale geometries, have impacted a diverse set of quantum optical applications ranging from optical quantum computing [2] to quantum communications [3] and sensing [4,5]. Like their electronic counterparts, the main benefit of integration in photonics platforms is the ease of cascading sequential operations while simultaneously scaling to large component numbers. Maintaining performance fidelity as the components scale to $O(1000)$ makes it inevitable to implement these devices in foundries [6,7]. Historically, these photonics foundries were driven mainly by classical data communication applications which dictated the choice of the starting silicon-on-insulator substrates to have silicon device layer thicknesses of 220 nm and standard waveguide cross-sections of ≈500 nm by 220 nm with a view toward single mode operation at 1.55 μm, maximizing component density and high-speed performance [8].

This strong sub-μm modal confinement brings with it challenges with surface absorption [9,10] and scattering [11] and the propagation loss of state-of-the-art foundry platforms has plateaued at ≈1 dB cm^{-1} [12]. The loss-tolerance metrics for quantum systems, especially at scale, are significantly worse than classical equivalents. This is perhaps best exemplified by the move of large-scale integrated photonic quantum computing platforms [12,13] from silicon to silicon nitride, despite the significantly weaker material nonlinearity [9]. Silicon, as a semiconductor, still has significant material advantages in terms of incorporating active devices, and therefore, our main question in this work is to investigate the prospects of silicon for integrated quantum photonics if waveguide loss can be significantly minimized by moving to thicker waveguide geometries wherein surface effects are relatively suppressed.

We study photon pair generation via spontaneous four wave mixing (SFWM) in microring resonators [14] fabricated via VTT's 3 μm silicon photonics foundry platform [15]. Employing hydrogen annealing [16] to smooth the fabrication-induced waveguide sidewall roughness, a low propagation loss of ≈2.7 dB m^{-1} (≈50× lower than 220 nm foundries) was achieved in this platform. In SFWM, two pump photons at frequency ω_p annihilate in the ring resonator to produce signal (ω_s) and idler (ω_i) photon pairs preserving energy and momentum conservation, with their frequencies aligned to the cavity resonances.

The figure of merit, the photon pair generation rate (PGR) [Hz], is given by [14,17]:

$$PGR = (\gamma 2\pi R)^2 \left(\frac{Q v_g}{\omega_p \pi R}\right)^3 \frac{v_g}{4\pi R} P^2, \tag{1}$$

where R is the (equivalent) radius of the microring resonator that corresponds to the total path-length of the racetrack resonators studied here, ω_p is the (angular) pump frequency [rad s^{-1}], v_g is the group velocity at the pump wavelength, Q is the loaded quality factor of the resonator, γ is the intrinsic mode nonlinearity—related to the mode effective area by $\gamma \propto \frac{1}{A_{eff}}$, and P is the pump power detailed below. For a fixed P, the PGR scales as $\propto Q^3/R^2 A_{eff}^2$ which introduces a nonlinearity-loss-footprint tradeoff. Increasing the waveguide thickness helps increase PGR, due to an increased Q, but also simultaneously decreases PGR, due to a decrease in γ and an increase in radiation loss limited minimum bending radius [18]. Understanding this nonlinearity-loss-footprint tradeoff is the main goal of this work.

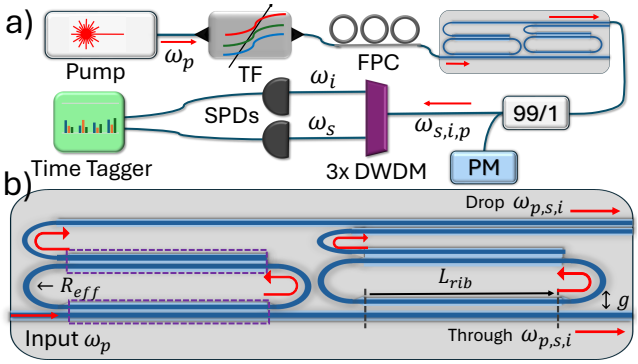

Fig. 1. (a) Schematic of the experimental setup used for resonator-based photon pair source characterization. DUT, device under test; DWDM, cascaded (3×) dense wavelength division multiplexers; FPC, fiber polarization controller; PM, power meter; SPD, superconducting single photon detectors (SPDs); TF, tunable filter. (b) Layout of the chip showing cascaded ring resonators coupled to the bus waveguide. The photon statistics are measured in the drop port. The three main resonator geometrical parameters varied in the experiments: bend radius (R_{eff}, we study two different radii here: Big Ring (BR) and Small Ring (SR)), rib waveguide length (L_{rib}) and waveguide resonator gap (g) are indicated.

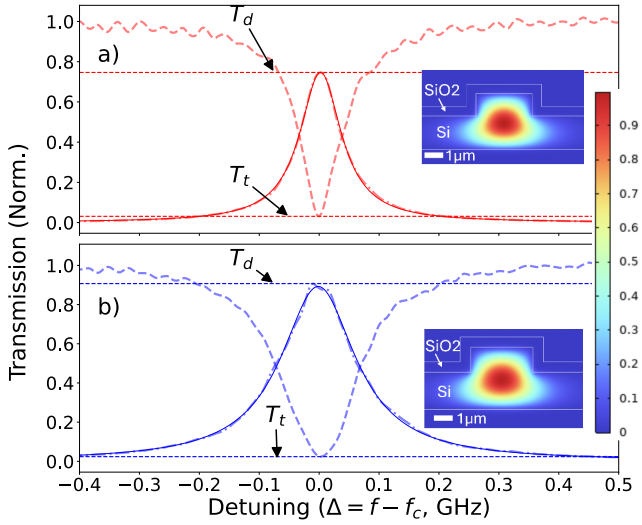

Fig. 2. Transmission spectrum of the TM mode (top, red) and TE mode (bottom, blue) of a representative ring resonator measured in the through (dashed) and drop (solid) ports. The (normalized) peak extinction and transmission is indicated by T_t and T_d. The normalized electric field profiles are shown in the inset. We extract a loaded Q of 1.28×10^6 (TE) and 2.29×10^6 (TM) by fitting a Lorentzian lineshape to the spectrum.

The schematic of our pair source characterization setup is shown in Fig. 1(a). A telecommunications band tunable laser (Santec TSL-550) is used as the pump source for the pair generation, and is filtered via a tunable fiber Bragg grating (AOS GmbH) to reduce residual pump noise in the signal and idler channels. The pump polarization is adjusted via a fiber polarization controller and is coupled onto the chip using a lensed fiber which provides mode matching at the waveguide facet. We measure a coupling loss of ≈1.8 dB per coupler (Section 1 of Supplement 1). The light is coupled from the bus waveguide into microring resonators and the generated signal and idler photon pairs are measured in the drop port of the resonator. Nominally identical rings with different waveguide-resonator coupling gaps are measured to quantify the PGR dependence on the ring's loaded quality factor (Q).

Cascaded dense wavelength division multiplexers (DWDMs) are used to filter out the pump photons from the signal and idler photons in the drop port. We measure a net pump suppression of 118.47 dB in our experiment by cascading 3× DWDM filters (Section 5.1 of Supplement 1). The signal and idler channel outputs of the DWDM are sent to two superconducting nanowire single-photon detectors (SPDs). The detector electrical outputs are read by coincidence counting electronics (Swabian Instruments), which records the signal, idler, and coincidence counts.

Figure 2 shows a representative microring resonator transmission spectrum measured in the through (dashed) and drop (dash-dot) ports for a pump wavelength of 1547.64 nm. The racetrack resonators, schematically shown in Fig. 1(b), are identical to the designs reported in [16]. They are designed with single-mode straight rib waveguide sections with a rib width of 3 μm and etch depth of 1.2 μm. The bends in the resonator are designed as strip waveguides to minimize the bend radii [18]. Two racetrack resonator designs with effective Euler bend radii (R_{eff}, Fig. 1(b)) [18] of 134.3 μm (small ring, SR) and 268.9 μm (big ring, BR) are studied here. The straight waveguide sections for the two R_{eff} are (L_{rib}, Fig. 1(b)) are 6.6 mm and 11.6 mm, respectively giving the resonators a free spectral range (FSR) of 9.1 GHz (SR) and 5.3 GHz (BR). Three identical copies of the SR and BR resonators are coupled to a bus waveguide with varying waveguide resonator coupling gap (Fig. 1(b)). Each resonator supports both transverse electric (TE) and transverse magnetic (TM) modes, shown by the blue and red curves in Fig. 2. We find the TM modes in general to have higher loaded Q's than equivalent TE modes [16]. For a given pump (and signal/idler) DWDM channel setting, we therefore have 12 (2 sizes × 3 gaps × 2 modes) variations to study the PGR dependence on R and Q. In addition, we have one all-pass ring which gives us 2 further data sets.

Figure 3 shows the measured signal (S), idler (I), and coincidence count (CC) rates for the TM mode (cf. Fig. 2) of a racetrack resonator of overall length 8.62 mm. Because of the spectral width of the DWDM filters (100 GHz), the signal and idler channel counts referred to here are not single resonator modes but correspond to ≈10 modes accounting for the resonator FSR (Section 4 of Supplement 1). This multi-mode nature doesn't affect our results as the key parameter of interest for this work, the PGR, is calculated as a ratio between the CC and S, I rates. To facilitate comparisons of PGR across resonators with different waveguide-resonator coupling gaps, the S, I, and CC curves are plotted with respect to $P_{WG}(1-\sqrt{T_t})$, where P_{WG} is the power in the bus waveguide measured off-cavity resonance and T_t is the minima of the normalized resonator mode transmission measured in the through port, as shown in Fig. 2. As the intracavity circulating power (P_{cav}), which underpins the photon pair generation is given by $P_{cav} = \frac{\mathcal{F}}{\pi} P_{WG}(1-\sqrt{T_t})$ with $\mathcal{F}$ representing the cavity finesse, this power scaling is necessary for fair comparison across devices.

To extract the PGR, we fit the measured S, I, and CC data to a quadratic function of power ($aP^2 + bP + c$), where $P = P_{WG}(1-\sqrt{T_t})$, cf. Section 4 of Supplement 1.The PGR is then

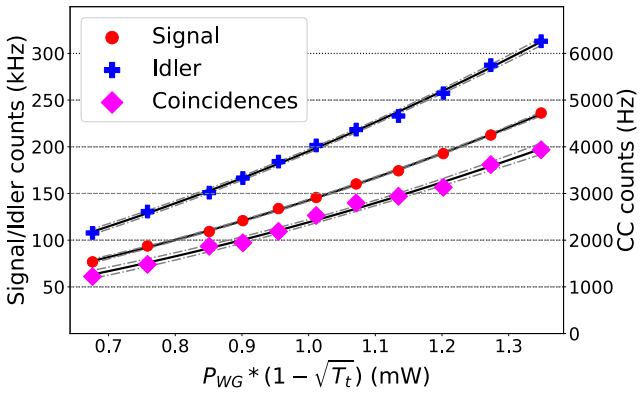

Fig. 3. Extracted signal, idler (left y-axis) and coincidence (right y-axis) count rates plotted as a function of coupled power for the TM mode shown in Fig. 2. The quadratic fits are shown by solid lines.

extracted as $a_s a_i / a_{cc}$ where s, i, cc represents the a coefficient of the respective quadratic fit to the S, I, and CC curves. Quadratic fits to the data in Fig. 3 are shown by solid black lines and the 95% confidence intervals are indicated by dashed lines. As multiple rings are cascaded on the same bus waveguide, the P_{WG} for each ring in series is estimated using a procedure detailed in Section 1 of Supplement 1. We measure an overall insertion loss of 7.87 dB from chip to detector. Using the extracted PGR, we can infer γ from Eq. (1). For the 3 μm devices, we extract an average γ of 4.71 m^{-1} W^{-1} across 11 devices. This agrees reasonably well with the estimated γ of 4.21 m^{-1} W^{-1} calculated using $\gamma = \frac{2\pi \overline{n_2}}{\lambda A_{eff}}$, where the $\overline{n_2}$ is weighted between silicon ($n_2 = 4.84 \times 10^{-18} m^2 W^{-1}$) and SiO_2 ($n_2 = 2 \times 10^{-20} m^2 W^{-1}$) accounting for the modal field distribution [19]. For reference, a 220 nm resonator pair source [20] gives us a γ of 190 m^{-1} W^{-1}.

Figure 4(a) plots the measured PGR/P^2 [Hz W^{-2}] scaled by the square of the equivalent ring radius R as a function of the loaded Q for the corresponding resonator. As expected from Eq. (1), we see a cubic dependence on Q, indicated by the linear fit of slope 3 in the log-log plot, across a range of device sizes and for both TE and TM modes. We are only able to report 11 measurements of the 14 potentially available, as the highest Q rings do not provide us with sufficient counts to get reliable statistics. In addition to the add-drop ring resonators where the photon pair statistics was measured in the resonator drop port, we also measured a standard all-pass ring resonator (shown by the purple star in Fig. 4(a)), which also agrees well with the Q^3 dependence [23]. Also shown (triangles) are data-points corresponding to 220 nm × 500 nm ring resonators [20–22]. Figure 4(a) clearly illustrates the nonlinearity-loss-footprint tradeoff. The 220 nm rings have significantly higher mode nonlinearity (γ) and allow tighter bends (lower R) which means that, for a given quality factor, the effective pair generation rate can be significantly higher as shown by the dashed magenta curve in Fig. 4(a), despite the R^2 scaling of PGR applied. In practice, the Q that can be achieved from such foundry availed ring resonators are $< 2.5 \times 10^5$, which limits the achievable PGR.

An alternative way to see the same tradeoff is to plot the PGR [Hz] for a fixed pump power (1 mW) in the bus waveguide. On cavity resonance, the intracavity circulating power (P_{cav}) is related to the power in the bus waveguide (P_{WG})

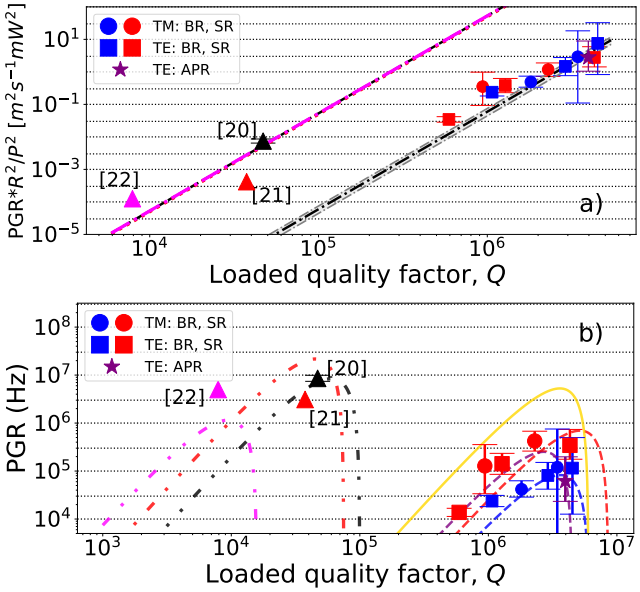

Fig. 4. (a) Q^3 scaling of the PGR rate across different resonator geometries is shown by plotting the PGR scaled by R^2/P^2. The dashed black line has a slope of 3; the grey dashed lines indicate 95% confidence intervals. APR, all pass ring; BR, big ring; SR, small ring; cf. text. Triangle markers show data from 220 nm devices taken from the literature [20–22]. (b) Measured and predicted PGR [Hz] for the measurements in (a) for a bus waveguide power of 1 mW, plotted as a function of device Q. The dashed blue, red, and magenta curves correspond to BR, SR, and APR 3 μm devices with the TE and TM mode data indicated in the legend. The dash-dot magenta, red, and black curves correspond to 220 nm devices. The gold curve corresponds to the predicted PGR of the optimal APR in the 3 μm platform, cf. text for details.

by $P_{cav} = P_{WG} \frac{4\kappa_e}{\kappa^2} \frac{v_g}{2\pi R}$ where κ_e is the waveguide cavity (power) coupling rate and $\kappa = \kappa_i + \Sigma \kappa_e$ is the total cavity decay rate. The cavity decay rate is related to the quality factor by $Q = \omega / \kappa$, where ω is the cavity resonance frequency [rad s^{-1}]. In an all-pass ring resonator, for a fixed intrinsic loss rate (κ_i), increasing κ_e increases the PGR, and it is maximized when the cavity is slightly close to overcoupling ($\kappa_e \approx \kappa_i$) [24]. At the two extremes of under-coupling and over-coupling, the PGR drops due to the cavity becoming decoupled from the waveguide ($\kappa_e \approx 0$) and the reduction in loaded Q due to over-coupling which reduces P_{cav}. This is shown graphically by the colored dashed lines in Fig. 4(b) for the 3 μm and 220 nm devices. We note that the same effective PGR can be obtained in two different scenarios, wherein a sufficiently high Q can compensate for a lower γ and larger R.

Equation (1) clearly shows that, for a fixed pump power P, the maximum PGR is ultimately set by Q once the waveguide geometry (γ) and implicitly the resonator size (R) are fixed by the specifics of the foundry platform via the $Q^3 / R^2 A_{eff}^2$ scaling. The add-drop resonators considered in this work are not optimal as single photon sources as Q is reduced corresponding to all-pass resonators of the same size by the presence of an additional decay channel. If we design a 3 μm all-pass ring to have the minimum radiation loss limited footprint ($R = 581$ μm) and use the expected intrinsic Q of 6×10^6 [16], for a fixed pump power of 1 mW in the bus waveguide, the maximum PGR is expected to increase by ≈10× over the present work, and becomes compa-

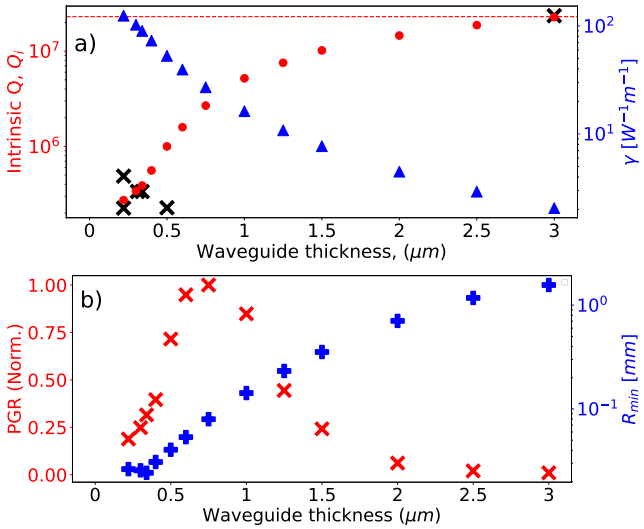

Fig. 5. (a) Dependence of intrinsic Q_i and mode nonlinearity γ on waveguide thickness, cf. Section 6 of Supplement 1 for model details. The experimental loss data available from foundries is shown by the black crosses. (b) Dependence of radiation loss limited bending radius R_{min}, cf. Section 6.1 of Supplement 1 on thickness and the normalized PGR showing a peak around 750 nm.

rable to the PGR of 220 nm devices [20]. We reiterate that this surface loss constraint on thin silicon platforms is practical, determined by photolithography [25], and not fundamental but has a disproportionate impact on quantum devices.

While the discussion so far has focused on tradeoffs associated primarily with linear optical loss for a fixed bus waveguide power, Eq. (1) shows that the pump power P is a free parameter and can be used to increase the net PGR. P is usually set by the requirement of keeping the multi-photon emission probability below a certain threshold [20]. As a reference, the nonlinear (two-photon) loss threshold is expected to be ≈10× lower than standard 220 nm devices on account of the increased A_{eff} [26]. The higher Q also modifies the spectral content of the photon wavepackets. High Q cavities will emit narrowband photons which could have significant advantages in matching the absorption spectrum of telecom band quantum emitters [27] and have the right spectral content for mapping quantum states from the microwave to the optical domain [28]. The lower dissipation should also lead to a higher heralding efficiency [24], which we are not able to validate here.

The discussion above naturally leads to the question of what the optimal device layer thickness should be for integrated silicon photon pair sources designed around microring resonators, accounting for this $\gamma^2 Q^3/R^2$ scaling and the practical surface loss constraint. While answering this question in general is difficult without resorting to detailed numerical simulations, one can construct simplified models to get insight into the scaling of Q, γ, and R with silicon thickness. The Q dependence on thickness can be estimated by calculating the surface roughness-induced scattering rate [29] and using the measured dissipation of 2.7 dB m^{-1} [16] in 3 μm waveguides as representative of background absorption, assuming negligible surface scattering. By noting that the total dissipation is the sum of the scattering and background absorption rates, we can extract the Q dependence on thickness as shown in Fig. 5(a), cf. Section 6.3 of Supplement 1 for details.

Similarly, the radiation loss limited bending radius R_{min} can be approximated for rib waveguide geometries [30] with varying silicon thickness and is shown in Fig. 5(b). With these assumptions, we can provide a (simplified) estimate for the normalized PGR as a function of device layer thickness and we find that the PGR is maximized for a silicon thickness ≈750 nm. While some of the analytical models are extended beyond their domain of strict validity, cf. Section 6 of Supplement 1, the qualitative trends are correct and can be extended to other material platforms [17], where device layer thickness is not constrained by foundry specifications.

Funding. UK Research and Innovation (EP/Z000688/1); European Research Council (758843); European Innovation Council (ACTPHAST4R).

Acknowledgement. We thank Matteo Cherchi, Timo Aalto, Oliver Green, Hugh Barrett, and Rob Thomas for feedback.

Disclosures. The authors declare no conflicts of interest.

Data availability. Data underlying the results presented in this paper are not publicly available at this time but may be obtained from the corresponding author upon reasonable request.

Supplemental document. See Supplement 1 for supporting content.

REFERENCES

1. J. Wang, F. Sciarrino, A. Laing, *et al.*, Nat. Photonics **14**, 273 (2020).
2. T. Rudolph, APL Photonics **2**, 030901 (2017).
3. P. Sibson, J. E. Kennard, S. Stanisic, *et al.*, Optica **4**, 172 (2017).
4. J. P. Dowling and K. P. Seshadreesan, J. Light. Technol. **33**, 2359 (2015).
5. C. L. Degen, F. Reinhard, and P. Cappellaro, Rev. Mod. Phys. **89**, 035002 (2017).
6. R. Soref, IEEE J. Sel. Top. Quantum Electron. **12**, 1678 (2007).
7. A. Rahim, J. Goyvaerts, B. Szelag, *et al.*, IEEE J. Sel. Top. Quantum Electron. **25**, 1 (2019).
8. J. Witzens, Proc. IEEE **106**, 2158 (2018).
9. M. Gao, Q.-F. Yang, Q.-X. Ji, *et al.*, Nat. Commun. **13**, 3323 (2022).
10. S. Grillanda and F. Morichetti, Nat. Commun. **6**, 8182 (2015).
11. F. Morichetti, A. Canciamilla, C. Ferrari, *et al.*, Phys. Rev. Lett. **104**, 033902 (2010).
12. PsiQuantum team, Nature **641**, 876 (2025).
13. H. Aghaee Rad, T. Ainsworth, R. Alexander, *et al.*, Nature **638**, 912 (2025).
14. L. G. Helt, M. Liscidini, and J. E. Sipe, J. Opt. Soc. Am. B **29**, 2199 (2012).
15. T. Aalto, M. Cherchi, M. Harjanne, *et al.*, IEEE J. Sel. Top. Quantum Electron. **25**, 1 (2019).
16. Y. E. Marin, A. Bera, M. Cherchi, *et al.*, J. Light. Technol. **41**, 3642 (2023).
17. T. J. Steiner, J. E. Castro, L. Chang, *et al.*, PRX Quantum **2**, 010337 (2021).
18. M. Cherchi, S. Ylinen, M. Harjanne, *et al.*, Opt. Express **21**, 17814 (2013).
19. V. S. Afshar, T. M. Monro, and C. M. de Sterke, Opt. Express **21**, 18558 (2013).
20. I. I. Faruque, G. F. Sinclair, D. Bonneau, *et al.*, Opt. Express **26**, 20379 (2018).
21. E. Engin, D. Bonneau, C. M. Natarajan, *et al.*, Opt. Express **21**, 27826 (2013).
22. S. Azzini, D. Grassani, M. J. Strain, *et al.*, Opt. Express **20**, 23100 (2012).
23. K. Guo, X. Shi, X. Wang, *et al.*, Photonics Res. **6**, 587 (2018).
24. Z. Vernon, M. Liscidini, and J. E. Sipe, Opt. Lett. **41**, 788 (2016).
25. S. Y. Siew, B. Li, F. Gao, *et al.*, J. Light. Technol. **39**, 4374 (2021).
26. K. Ye, A. Keloth, Y. E. Marin, *et al.*, APL Photonics **10**, 026108 (2025).
27. A. Gritsch, L. Weiss, J. Früh, *et al.*, Phys. Rev. X **12**, 041009 (2022).
28. K. C. Balram and K. Srinivasan, Adv. Quantum Technol. **5**, 2100095 (2022).
29. J. Lacey and F. Payne, IEEE Proc. J. Optoelectron. **137**, 282 (1990).
30. E. Marcatili and S. Miller, Bell Syst. Tech. J. **48**, 2161 (1969).